6

Hydroxo-Methoxo Bridged Organostannoxane Based NDR Device

Research Article based on this study:

Mishra, A., Betal, A., Kumar, R., Lama, P., Sahu, S., and Metre, R. K., (2021), "Dinuclear Monoorganostannoxane $[(RSn^{IV})_2(\mu\text{-}OH)(\mu\text{-}OCH_3)Cl_4]\cdot CH_3OH$ (R= 2-(Phenylazo)phenyl) Assembled Using Intramolecular Coordination Approach: Design of Organostannoxane-Based NDR Device", *ACS Applied Electronic Materials*, Vol.3, No.1, pp.203–210.

6.1 Introduction

Molecular Materials and Devices have attracted considerable interest during the last few years. The successful applications of various devices such as organic light-emitting devices (OLED) [Beucher et al., 2020b; Gusev et al., 2019] and Field effect transistors [Wachi et al., 2017] have provided much-needed impetus in this area . Different areas involving research on photovoltaic devices [Brus et al., 2019], bioelectronics [Moser et al., 2019], printing [Cirelli et al., 2019] and flexible electronics [Hashemi et al., 2020; Raghuwanshi et al., 2019] has been continuously attracting interest for their great potential in solving energy-related challenges faced by today's information-driven society. In this context, researchers worldwide are targeting more efficient and smart devices. Various electronic devices such as light-emitting devices (LED) [Nguyen et al., 2020], Solar cells [Freitag et al., 2015], photo-detector [Freitag et al., 2015], transistors [Mahato et al., 2019], spintronic [Mahato et al., 2019], and photo controlled devices [Bhattacharyya et al., 2020] have been studied in the recent past and continue to gain worldwide attention. These devices can be easily fabricated on various surfaces with cost-effectiveness and easy processing via the solution method.

Among these, nonvolatile memory devices exhibiting negative differential resistance (NDR) effects are emerging as promising candidates to address various challenges existing in the field of molecular electronics. NDR devices exhibit the special property of a decrease in current with the increasing voltage. The applications of NDR-based devices span across broad areas such as Oscillators [Chow et al., 1998], Analog to Digital converters [Broekaert et al., 1998], logic circuits [Mathews et al., 1999], and memory devices [Chen et al., 2009].

A variety of materials that are actively investigated for such devices include mainly semiconductors [Tizno et al., 2019], organic compounds [SD et al., 2020], and polymers [Narasimhan Arunagirinathan et al., 2019]. Despite the unique electronic features and luminescence properties, coordination complexes, as well as organometallic complexes, are rather underexplored in the literature [Kundu et al., 2014b; Pandey et al., 2019]. Some of the materials studied for NDR behavior include a report by Liu *et al.* where they have reported an organometallic Molecular Double Dot (MDD) system consisting of cobaltocene and ferrocene, which showed negative differential resistance through the molecular level crossing [Liu et al., 2006]. Oberoi *et al.* reported a Fe(II) based polymer having redox non-innocent ligand, which exhibits NDR and memory behavior [Oberoi et al., 2018]. Zhang *et al.* reported a memory device

based on Au nanoparticles functionalized with TEDOT units which shows an NDR effect with a peak/valley ratio up to 17 [Zhang et al., 2017a]. Lin *et al.* reported a Zn phthalocyanine-based hybrid material doped with polystyrene, which shows NDR and memory effects [Lin et al., 2007]. Recently, Zou *et al.* reported the negative differential behavior of phosphorus-doped graphene nanoribbons [Zou et al., 2015].

On the other hand, molecular organotin complexes have been explored very widely in terms of their structure as well as applications in different areas such as biological activity [Devi et al., 2018; Joshi et al., 2020], gas sensors [Fu et al., 2017], ion sensors [Vinayak et al., 2019b], optical properties [Geringer et al., 2020], and counter electrode material in dye-sensitized solar cells [Cantón-Díaz et al., 2018] etc. A recent study from our research group reported a molecular organotin sulfide cage [$(RSn)_4S_6{\cdot}4H_2O.2CHCl_3$; R = *2-phenylazophenyl*] based device exhibiting the memristive behavior with excellent ON-OFF ratio 10^3 [Mishra et al., 2020]. In continuation of our research interests in the organotin-based molecular materials, herein we report the synthesis, structural characterization, and NDR behavior of monoorganostannoxane $[(RSn^{IV})_2(\mu\text{-}OH)(\mu\text{-}OCH_3)Cl_4]{\cdot}CH_3OH$ (R= 2-(phenylazo)phenyl) designed using the intramolecular coordination approach.

6.2 Experimental Section

6.2.1 Synthesis

$[(RSn^{IV})_2(\mu\text{-}OH)(\mu\text{-}OMe)Cl_4]{\cdot}CH_3OH$ (R = 2-phenylazophenyl) (4). A mixture of $RSnCl_3$ (0.10 g, 0.25 mmol) and NaOH (0.010 g, 0.25 mmol) in 20 ml of acetone/methanol (1:1) was stirred at room temperature for 4h. The suspension was filtered and kept for crystallization. Yellow colored crystals of complex **4** were successfully obtained within few days. Yield (Based on $RSnCl_3$): 0.080g (82%). M.P. > 210ºC. Elemental Analysis: anal. calcd. For $C_{26}H_{26}N_4O_3Sn_2Cl_4$ (821.8) C, 38.00; H, 3.19; N, 6.82; found C, 38.42; H, 3.08; N, 6.73. ^{1}H NMR (500MHz, $CDCl_3$, ppm): δ 8.09 (m), 7.81 (m), 7.54 (m), 3.48 (s, OCH_3). $^{13}C\{^1H\}$ NMR (125MHz, $CDCl_3$, ppm): δ 136.7, 136.2, 134.5, 132.9, 130.3, 129.7, 124.9, 51.2 (s, OCH_3). ^{119}Sn NMR (186MHz, $CDCl_3$, ppm): δ -439. ESI-MS: $[(RSn)_2(\mu\text{-}OMe)(\mu\text{-}OH)Cl_3.3CH_3OH]^+$, 848.963; IR (KBr, cm^{-1}): 3377 (br), 3061 (w), 2921 (s), 2852 (m), 1950 (w), 1564 (w), 1451 (s), 1310 (m), 1215 (s), 1004 (m), 777 (s), 680 (m), 540 (s), 435 (m).

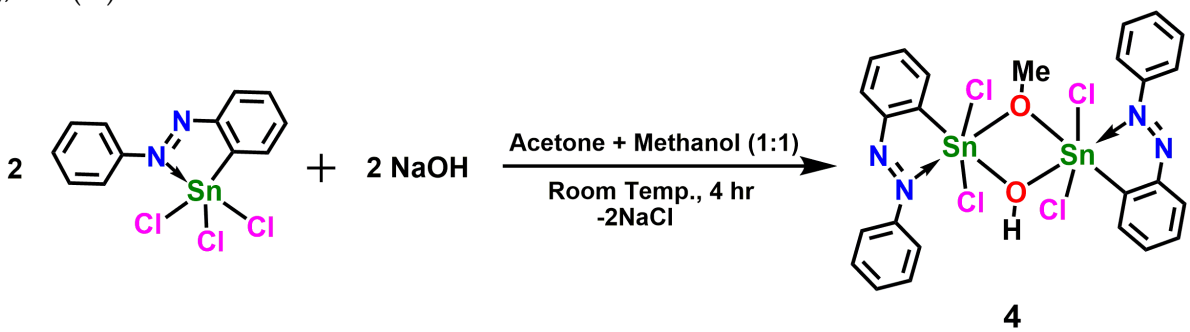

Scheme 6.1 Synthesis of complex **4**.

6.2.2 Single-Crystal X-ray Crystallography

The details pertaining to the data collection and refinement for **4** are given in Table 6.1.

Table 6.1 Crystal data and structure refinement parameters for complex **4**.

Identification code	**4**
Empirical formula	$C_{27}H_{30}Cl_4N_4O_4Sn_2$
Formula weight	853.78
Temperature/K	273(2)
Crystal system	monoclinic
Space group	Cc

a/Å	19.8469(15)
b/Å	10.9920(6)
c/Å	16.8212(13)
α/°	90
β/°	125.445(3)
γ/°	90
Volume/Å^3	2989.6(4)
Z	4
ρ_{calc}g/cm^3	1.826
μ/mm^{-1}	2.064
F(000)	1608.0
Crystal size/mm^3	0.250 × 0.210 × 0.180
Radiation	MoKα (λ = 0.71073)
2Θ range for data collection/°	6.134 to 49.998
Index ranges	-23 ≤ h ≤ 23, -13 ≤ k ≤ 13, -20 ≤ l ≤ 20
Reflections collected	17589
Independent reflections	5254 [R_{int} = 0.0251, R_{sigma} = 0.0272]
Data/restraints/parameters	5254/2/360
Goodness-of-fit on F^2	1.030
Final R indexes [I>=2σ (I)]	R_1 = 0.0163, wR_2 = 0.0377
Final R indexes [all data]	R_1 = 0.0170, wR_2 = 0.0381
Largest diff. peak/hole / e Å^{-3}	0.71/-0.28

6.2.3 Device Fabrication

Indium Tin Oxide (ITO) coated glass substrates were bought from Techinstro and were used for the fabrication of the two-terminal device, which was first etched to make a thin strip in the middle portion of the substrate. Concentrated hydrochloric acid (HCl) and zinc (Zn) dust were used to etch the ITO coating from the glass substrate [Vyas et al., 2018b]. After etching, the substrates were cleaned by a well-known procedure of ultrasonication of substrate three times with soap solution for 15 min [Vyas et al., 2016]. After this, the substrates were cleaned using ultrasonication in acetone, deionized water (DI), and methanol three times each for 15 min. Cleaned substrates were kept overnight in an oven at 70°C.

Synthesized complex **4** was dispersed in chloroform at a concentration of 20 mg/ml, followed by 6 h of ultrasonication to get a homogeneous solution. This homogeneous solution was spin-coated at a speed of 2000 rpm on the cleaned substrate to get a smooth thin film. This thin film on the substrate was kept at 35°C for 6 h before being used for the deposition of the top metal contact. Aluminium (Al) wire purchased from Sigma-Aldrich was deposited on the active layer by the thermal deposition system to make the top electrical contact. A Shadow mask was used during deposition to get crossbar architecture and the deposited Al thickness was about 60 nm. So, the device structure is as follows: ITO/Complex **4**/Al. The schematic of the fabricated device is shown in Fig. 6.1. After the fabrication of the device, it was electrically characterized in a homemade probe station which is interfaced with a Keithley 6430 Femto ampere source meter.

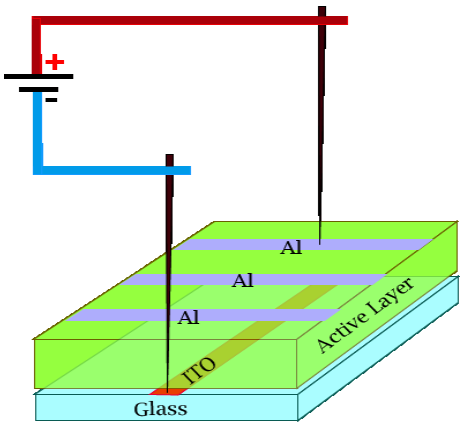

Fig. 6.1 The schematic diagram of the crossbar architectured device in which ITO is the bottom contact and Al is the upper contact for electrical characterization.

6.2.4 Theoretical Calculations

Gaussian 09 and ORCA software used for the calculations and the methodology used here are the same as in our previous report [Mishra et al., 2020]. In TDDFT, the solvent effect was considered using CPCM method with DCM.

6.3 Results and Discussion

6.3.1 Synthetic Aspects

Complex **4** is prepared by the room temperature reaction of $RSnCl_3$ (R= 2-phenylazophenyl) and sodium hydroxide in acetone/methanol (1:1) in a stoichiometric ratio (Scheme 6.1). Suitable single-crystals of **4** for X-ray diffraction analysis were obtained as its methanol solvate **4**·CH_3OH by slow evaporation of its acetone/methanol solution. During the partial hydrolysis, some of the chlorides were exchanged by μ-hydroxo and μ-methoxy ligands, which were further confirmed by the Single-Crystal X-ray diffraction analysis, FTIR, and NMR spectroscopy. The ^{119}Sn NMR spectrum of complex **4** showed a single signal at -439 ppm, which indicates both the Sn centers present in **4** are in the same chemical environment. It showed multiplet signals in the

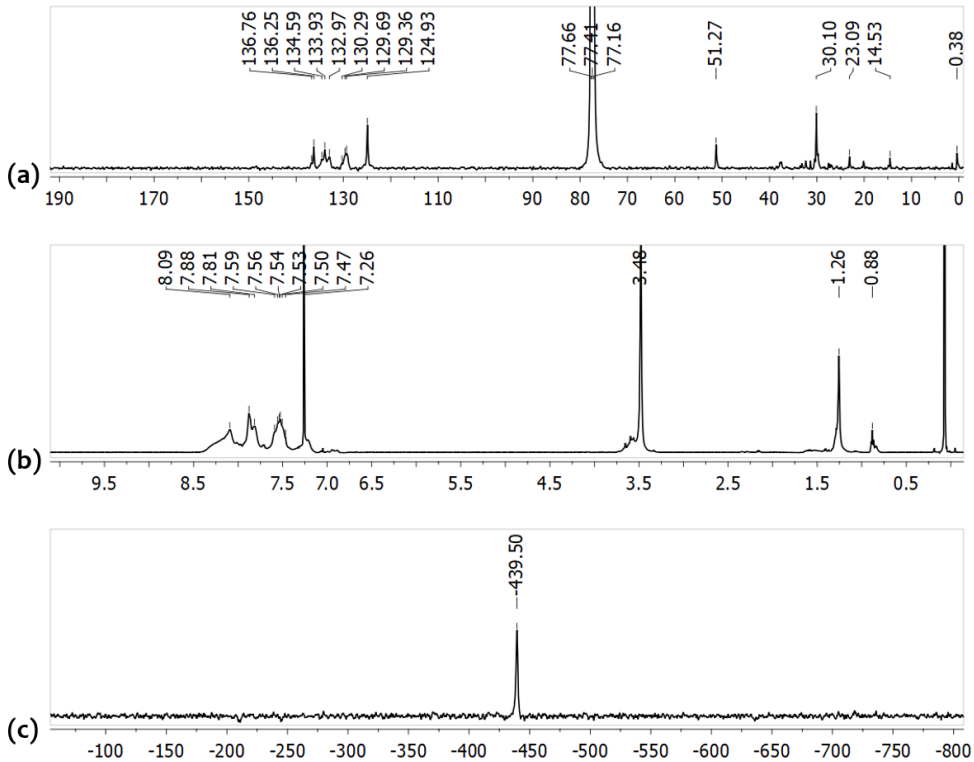

Fig. 6.2 (a) ^{1}H NMR, **(b)** ^{13}C NMR and **(c)** ^{119}Sn NMR of complex **4** recorded in $CDCl_3$.

range of δ 7-9 ppm in the ^{1}H NMR spectrum due to the aromatic protons associated with the ligand attached to the Sn center, and a signal at δ = 3.5 ppm is attributed to the protons of μ-methoxy ligand in the structure (Fig. 6.2). FTIR spectrum showed a broad peak at 3377cm^{-1} owing to the presence of the hydroxo group in the complex. ESI-MS studies reveal that under ESI-MS conditions, **4** undergoes fragmentation with the absence of molecular ion peak. However, the mass cluster centered at m/z 848.963 can be assigned to a fragment $[(RSn)_2(\mu\text{-}OMe)(\mu\text{-}OH)Cl_3.3CH_3OH]^+$. Thermogravimetric analysis revealed that complex **4** is stable up to 220 °C, then it undergoes sudden weight loss followed by gradual weight loss up to 380 ºC (Fig. 6.3).

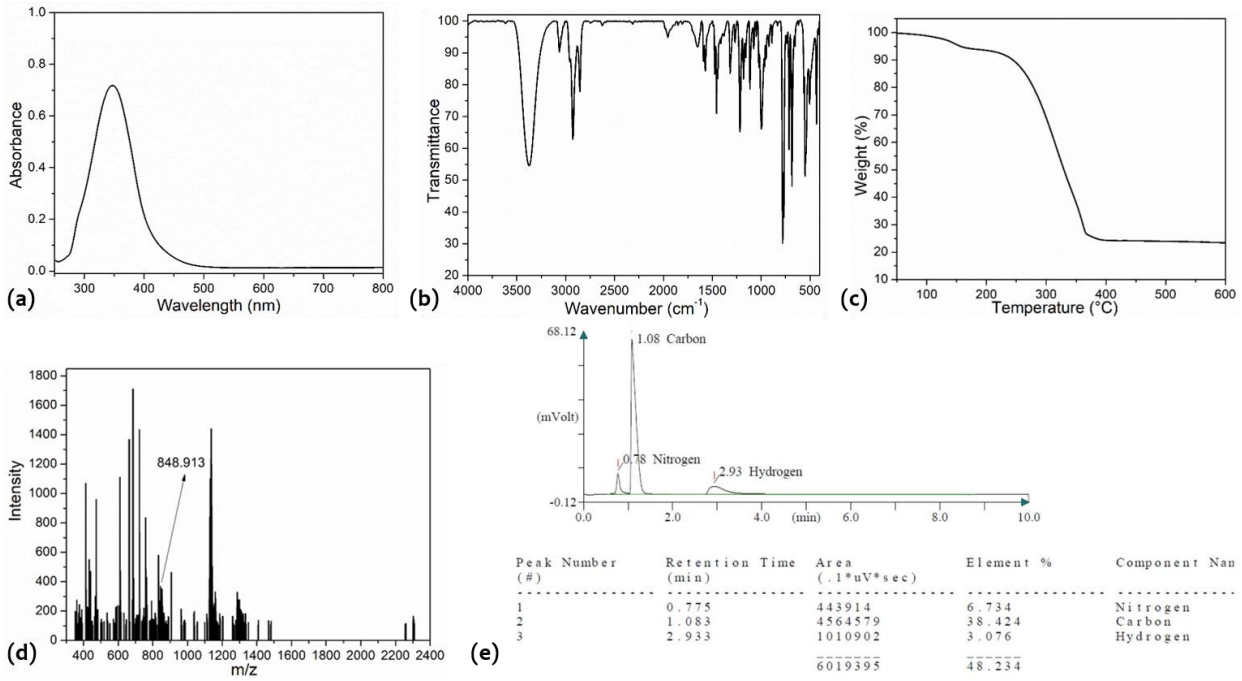

Fig. 6.3 (a) FTIR spectrum, **(b)** UV-Vis spectrum (conc. 10^{-5}M in $CHCl_3$), **(c)** TGA (under N_2 atmosphere) **(d)** ESI-MS spectrum and **(e)** CHN analysis of complex **4**.

6.3.2 Molecular and Supramolecular Structure of Complex 4

The crystal structure of complex **4** is shown in Fig. 6.4(a). Complex **4** belongs to a large structural family of organotin complexes containing Sn-O units called organostannoxanes [Chandrasekhar et al., 2002b]. In complex **4**, the two tin atoms (Sn1 and Sn2) are held together by bridging coordination action from a μ-hydroxy and μ-methoxy ligands to generate a central $[Sn_2(\mu\text{-}OH)(\mu\text{-}OMe)]$ core (Sn2-O1, 2.0251(3)Å; Sn2-O2, 2.2214(3)Å; Sn1-O1, 2.1625(3)Å; Sn1-O2, 2.0503(3)Å and average Sn-O-Sn, 109.28°) [Howie et al., 2011; Portnyagin et al., 2006]. These values are comparable with the literature precedents (average Sn−O 2.142 Å, Sn−O−Sn 109.54°). A report by Mehring *et al.* shows an organostannoxane with similar coordinating modes and hydroxy bridging, which has comparable bond parameters [Mehring et al., 2001]. Central $[Sn_2(\mu\text{-}OH)(\mu\text{-}OMe)]$ core present in **4** is a very uncommon core of the monoorganostannoxane family where two Sn centers are bridged by both μ-hydroxy and μ-methoxy ligands. In addition to the μ-hydroxy and μ-methoxy ligands, Sn1 and Sn2 are further coordinated to two terminal chloride ligands each. Interestingly, the formation of **4** is accompanied by retention of the intramolecular N→Sn coordination present in the starting precursor. Intramolecular N→Sn bond distances are comparable in **4** (average N→Sn, 2.442 Å) with that of $RSnCl_3$; average N→Sn 2.451 Å [Chandrasekhar et al., 2013a]. Closer inspection of the central core reveals that all the Sn and O atoms lie on the plane [Fig. 6.4(b)]. Each Sn atom in complex **4** is hexacoordinated [1C, 1N, 2O, 2Cl coordination] and present in a distorted octahedral geometry with the one N atom and one of the Cl atoms in the axial position [Fig. 6.4(c)].

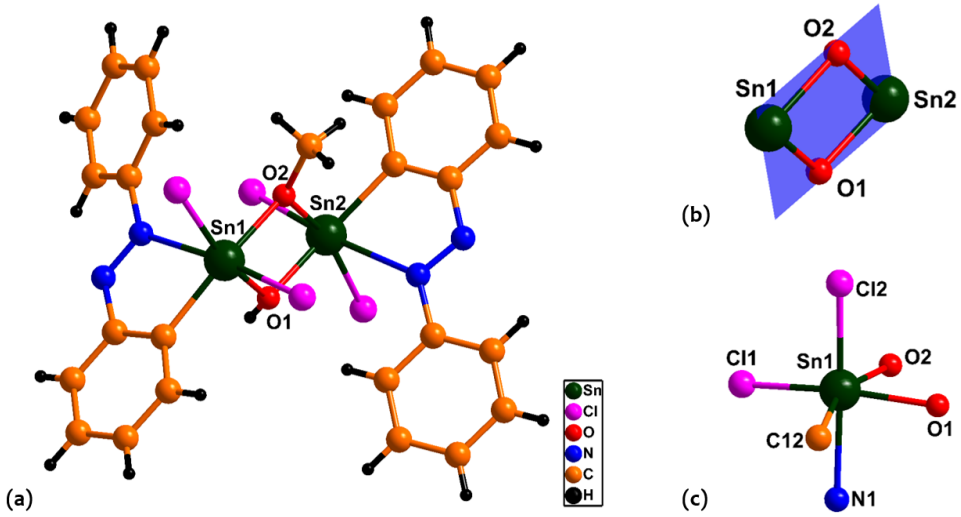

Fig. 6.4 (a) Molecular structure of complex **4**. Bond distance (Å) and bond angle (°) parameters: Sn2-O1, 2.0251(3)Å; Sn2-O2, 2.2214(3)Å; Sn1-O2, 2.0503(3)Å; Sn1-O1, 2.1625(2)Å; Sn1-O1-Sn2, 110.907(1)°; Sn1-O2-Sn2, 107.669(1)°; **(b)** Core structure with a molecular plane. **(c)** Coordination environment of Sn in complex **4**; Sn1-N1, 2.4015(7)Å; Sn1-C12, 2.1139(4)Å; Sn1-Cl1; 2.3935(1)Å; Sn1-Cl2, 2.4102(2)Å; O1-Sn1-O2, 71.078(1)°, N1-Sn1-Cl2, 173.935(1)°; N1-Sn1-C12, 73.468(1)°; Cl1-Sn1-Cl2, 95.699(5)°.

As per previous reports in the literature, organostannoxanes are known to show interesting supramolecular structures in solid-state. Studies of the crystal structure of complex **4** revealed the formation of one-dimensional and two-dimensional supramolecular architectures. These supramolecular structures are formed by the interactions like hydrogen bonding C-H…N, C-H…O, and C-H…π (Fig. 6.5 and 6.6) [Chandrasekhar et al., 2002a, 2005, 2007, 2010, 2013b; Metre et al., 2014].

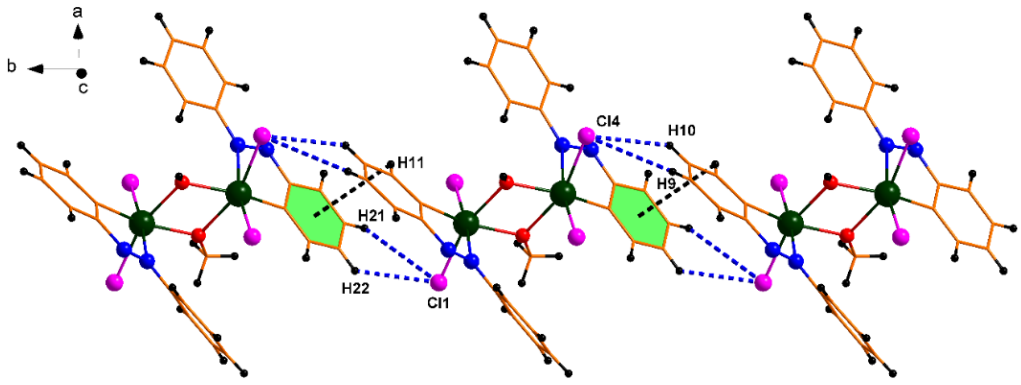

(a)

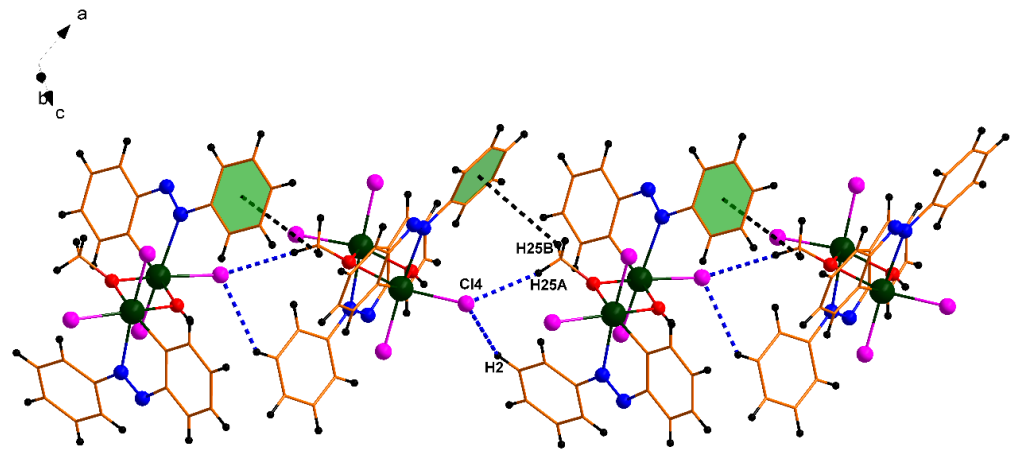

(b)

Fig. 6.5 (a) One-dimensional supramolecular assembly of **4** formed from C-H…π and CH…Cl interactions. Metric parameters are as follows; π-H11, 3.3861(2)Å; H21-Cl1, 3.5767(1)Å; H22-Cl1, 2.8670(1)Å; H9-Cl4, 3.5511(1)Å; H10-Cl4, 2.8765(1)Å **(b)** One-dimensional supramolecular assembly of **4** formed by C-H…π and C-H…Cl interaction. Metric parameters are as follows; π-H25B, 3.7914(3)Å; H25A-Cl4, 2.7698(1)Å; H2-Cl4, 3.0026(1)Å.

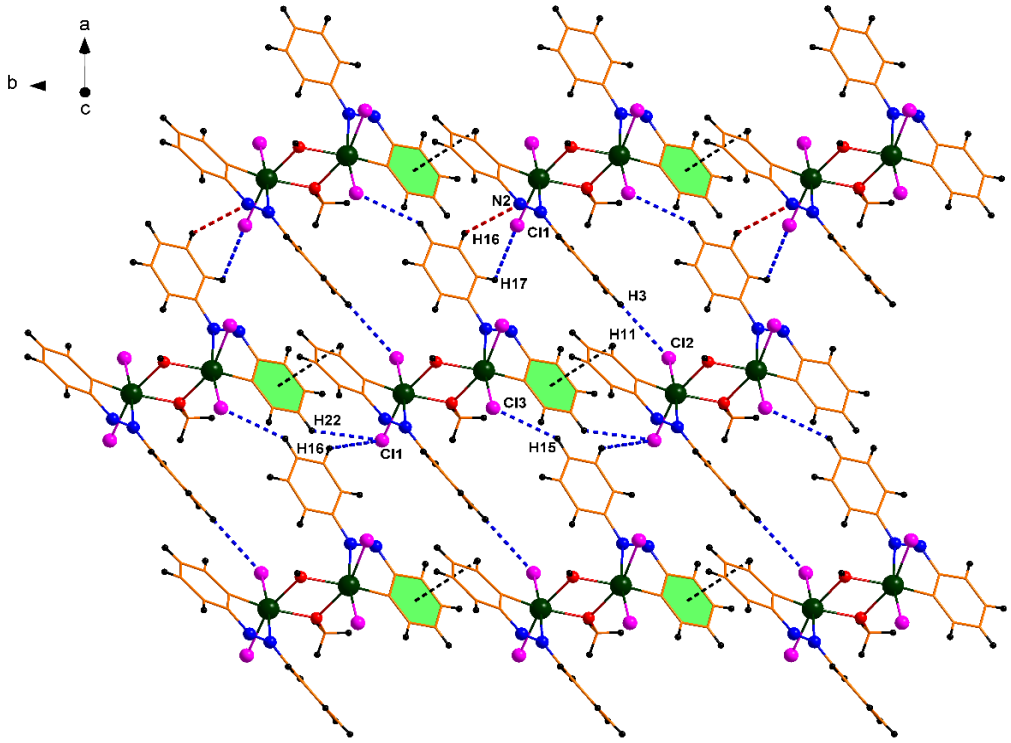

Fig. 6.6 Two-dimensional supramolecular architecture of **4** formed from C-H…π, C-H…N and C-H…Cl interactions. Metric parameters are as follows: π-H11, 3.3861(2)Å; H17-Cl1, 3.5806(1)Å; H3-Cl2, 3.0179(1)Å; H15-Cl3, 2.9103(1)Å; H16-Cl1, 3.2513(1)Å; H16-N2, 2.8670(1)Å.

6.3.3 Photophysical and DFT Studies

DFT studies were performed in collaboration. The UV-Vis spectrum of **4** (10^{-5} M conc. in dichloromethane) was recorded at room temperature. The UV-Vis spectrum shows mainly two absorption peaks, one at 348 nm with a larger extinction coefficient and another smaller at 285 nm. The peak at 348 nm may be associated with symmetry allowed π-π* transition based on 2-phenylazophenyl moiety. To fully understand these peaks, we have performed time-dependent density functional theory (TD-DFT) calculations on complex **4** [Dirac, 1929; Frisch et al., 2009; Neese, 2012; Perdew et al., 2018; Slater, 1951; Staroverov et al., 2003; Tao et al., 2003; Weigend et al., 2005]. TD-DFT calculations suggest three characteristic peaks at 325 nm, 373 nm and 436 nm, which are consistent with the experimental UV-Vis data (Fig. 6.7). Due to the broadness of the experimental spectrum, the peak at 436 nm is merged with 373 nm peak (Fig. 6.7). Based on the highest occupied molecular orbital (HOMO) and lowest unoccupied molecular orbital (LUMO), we have found the corresponding transitions related to these peaks. The high-intensity symmetry allowed a peak at 373 nm corresponds to two equal probability transitions from HOMO to LUMO+1 and HOMO-1 to LUMO, while the two low-intensity symmetry forbidden peaks at 325 nm and 436 nm correspond to HOMO-1 to LUMO+2 and HOMO-2 to LUMO respectively. As expected, the transition at 373 nm is found to be a π-π* transition based on 2-phenylazophenyl moiety (Fig. 6.7). The transitions at 325 nm and 436 nm are found to be π(Ligand)-σ*(Metal-Ligand) and π+σ (Ligand)-π*(Ligand), respectively, which are generally found to have a low extinction coefficient (Fig. 6.7). In the previous study [Mishra et al., 2020], we have found the HOMO to LUMO transition for high-intensity peaks, but this complex scenario is different (see the transition corresponds to the 373 nm peak shown above in Fig. 6.7).

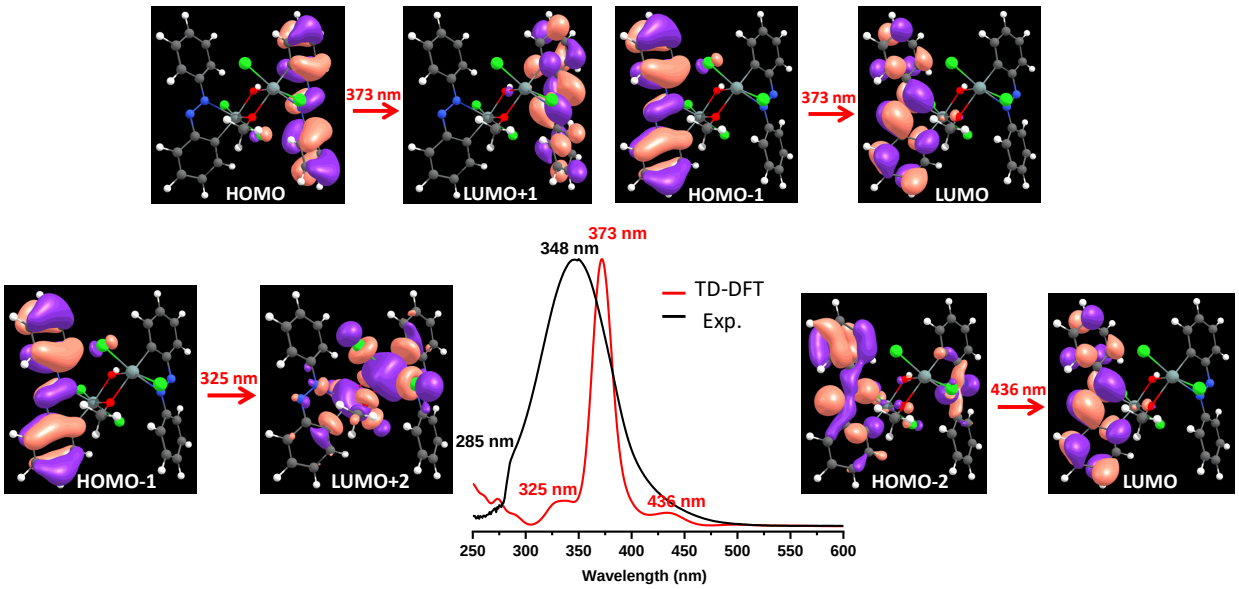

Fig. 6.7 A comparative absorption spectrum of complex **4** where experimental data is shown in black and TD-DFT computed data in red along with the corresponding orbital transitions.

As complex **4** shows a different transition for a high-intensity peak at 373 nm, it is important to look into the HOMO-1, HOMO, LUMO and LUMO+1 orbital energies. From the DFT calculations, we have found that the energies of HOMO-1, HOMO, LUMO and LUMO+1 are -6.57 eV, -6.54 eV, -3.54 eV and -3.51 eV, respectively. The energy gap between these two HOMO and two LUMO orbitals is very small (0.03 eV), which means they are almost degenerate. Due to this, the transitions occur in the same side ligand orbitals and not from one ligand to another ligand of complex **4,** which is the case for the HOMO to LUMO transition (Fig. 6.7). The HOMO-LUMO gap for this complex is 3.00 eV and the HOMO and LUMO pictures are given in Fig. 6.7. As the π-conjugated system with a suitable HOMO-LUMO gap is investigated for the negative differential resistance (NDR) properties [Lin et al., 2007; Oberoi et al., 2018; Seminario et al., 2000; Zhang et al., 2017a], we thought to screen some preliminary properties of this molecule towards the NDR using DFT.

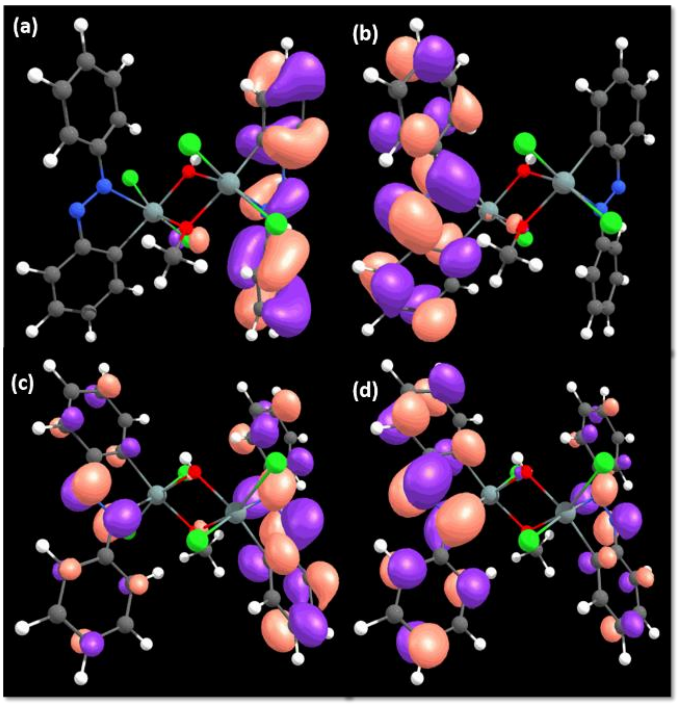

Fig. 6.8 Molecular orbital diagram of complex **4** **(a)** HOMO and **(b)** LUMO with its singly reduced form **(c)** SOMO and **(d)** LUMO orbital pictures. The orbital with orange color represents the alpha orbital and the violet color with a beta orbital. The contour value used to plot these is 0.03 a.u.

To compute the NDR properties, we have first calculated the singly reduced species of complex **4**. The singly reduced species SOMO (singly occupied molecular orbital) and LUMO diagram are shown in Fig. 6.8, which suggests a complete change in the spatial distribution of frontier orbitals for both neutral and reduced molecules of complex **4**. The computed singly reduced species of complex **4** suggests an increase in the bond length of azo group nitrogen from 1.257 Å to 1.281 Å (1.300 Å). An overlay diagram shown in Fig. 6.9 reveals the change in the torsion in the aromatic benzene ring after reduction. The change in the spatial distribution of the Frontier orbital indicates the molecular electron transport. Due to the changes occurring in frontier orbitals and torsion in the aromatic rings, the resistance increases, which corresponds to the NDR effect observed in the devices [Dagar et al., 2019; Seminario et al., 2000]. The HOMO-LUMO gap is reduced from 3.00 eV to 0.20 eV in the singly reduced species of complex **4**.

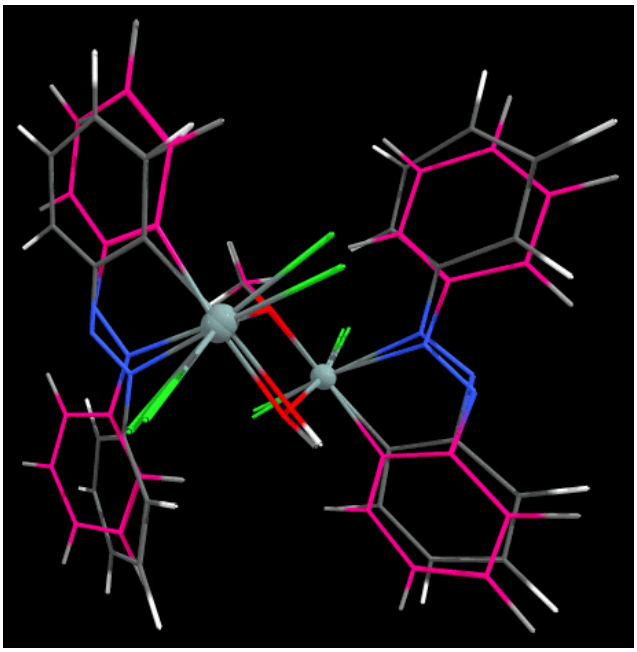

Fig. 6.9 Overlay diagram of complex **4** with its reduced species. Note, here; the grey carbon structure is for complex **4** while the pink carbon structure is for singly reduced species.

6.3.4 NDR Studies

Device studies were performed in collaboration. The I-V characteristic of the device has been studied by applying a voltage to the device to check the electrical properties of the material. The current versus voltage characteristic is shown in Fig. 6.10, in which voltage was scanned from 0V to 3.2V, then returned to 0V, and again voltage increases to -3.2V finally came to 0V with a scan speed of 0.02 V/S to complete a full cycle. The current path of the full cycle is guided by the arrows (red). The current increase when the voltage increases up to 1.5V and reaches a peak, which gives the local maxima. After that, the current decreases to a valley as voltage increases further to 2.5V, and the trend continues till 3.2V. The device remained in the low conducting state when the voltage went back to zero. So a negative differential resistance (NDR) behavior was from the device in the region of 1.5V to 2.5V. When the voltage was traced from 0 to negative voltage side current reached compliance (10mA) at -2.08V and a further increase in voltage kept the current at the compliance level only. While tracing back from -3.2 V to 0 V, the current remains at compliance up to -2.3V and starts decreasing through the low conduction path to zero. Hundreds of such iterations were carried out to confirm the property of the material, and every time it showed the same behavior. The on-off ratio changes with voltage, logarithmic current with voltage plot is shown by the upper and lower inset Fig. 6.10 (a),(b), respectively. The ratio between on and off state is maximum at 1.5 V, which is the peak of the current versus voltage curve. Fig. 6.10(b) shows two different paths of current along the positive side but along the negative side during trace and retrace; the current difference between the two states is very small.

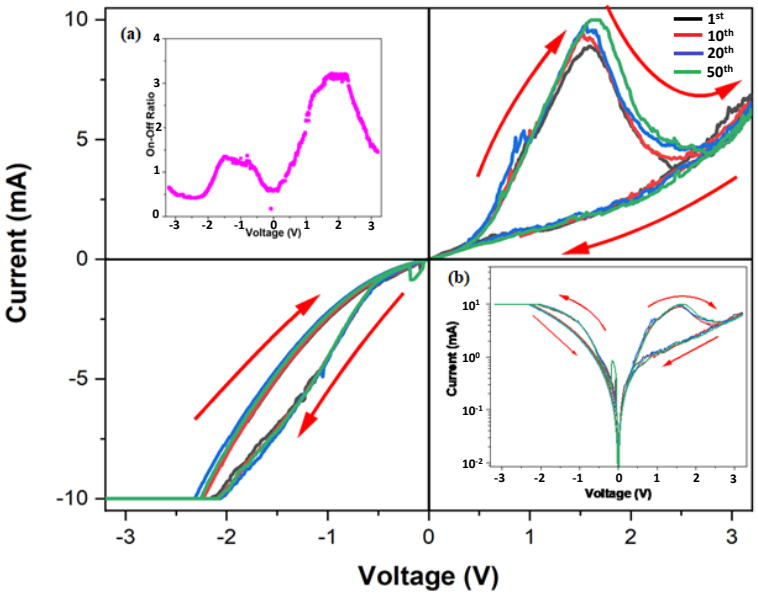

Fig. 6.10 Current-Voltage and NDR characteristics plot of the device. The red arrows showed the current path during the full I-V cycle. The current starts increasing to reach peak maxima and valley minima at 1.5V and 2.5V, respectively. The 1st, 10th, 20th, and 50th I-V cycles are plotted here. The current ratio between on-state and off-state is given in the upper inset fig. **6.10(a)**. The logarithmic plot of current and voltage is shown in lower inset fig. **6.10(b).**

With NDR behavior, hysteresis was also seen from the I-V curve of the device, which indicates the material is a potential candidate for a resistive memory device, so memory switching characterization was carried out. Random-access memory (RAM) behavior of the device was tested with -3.2V, 3.2V, 1.5V for 10 s each as write, erase and read voltage, respectively. RAM behavior has been studied for up to 40000 s, and the device shows stable behavior for the two states. The input voltage and output current varying with time are shown in Fig. 6.11(a). The figure shows that at -3.2V, the device reaches compliance current (10mA) to set the resistance from high to low, and at 3.2V, the reverse process happens. So, after erasing the pulse when the data was read by applying a pulse voltage of 1.5V, the device went to the low conducting state. After applying -3.2V, when the state is probed at 1.5 V, the device went to a high conduction state. The stability of the device has been checked by studying data retention, as shown in Fig. 6.11(b). Retention for about 2000 s of each state has been checked. To check to write state or high conducting state at first, a write pulse of -3.2V was given for 10 s to set the device to high current, and after that, a voltage pulse of 1.5V was given to read whether the state could retain or not. Similarly, for checking the retention of a high resistant state or low conducting state, an erase voltage of 3.2V for 10 s was given to the device and read the state at the same read voltage of 1.5V in which it remains in the low conducting state.

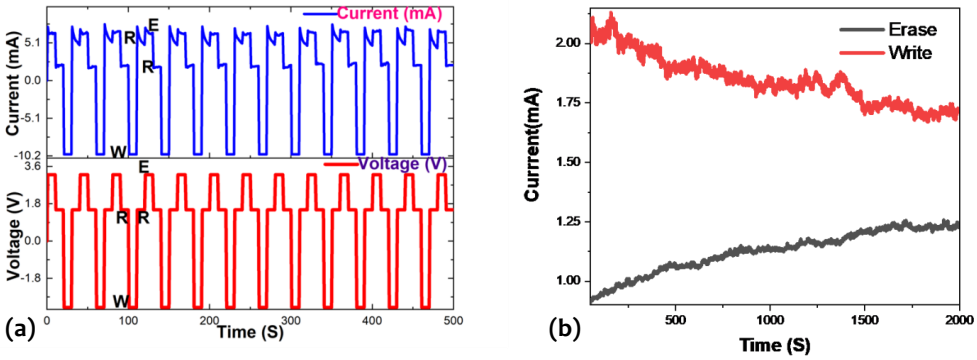

Fig. 6.11 (a) RAM behavior of the device with write, read, erase voltage of -3.2V, 1.5V, 3.2V, respectively, for 10 s each. Voltage vs. time (red color) and current vs. time (blue) plots were shown. **(b)** retention of the device checked up to 2000 s with the read voltage 1.5V and-3.2V, 3.2V as the write and erase voltages, respectively. The device retains its state the whole time.

The surface structure plays a crucial role in explaining the features of the device, and in our case, also we checked that by studying the surface morphology of the device. The surface characteristics were checked by Park system XE 70 Atomic Force Microscopy (AFM). The thin film was prepared on a previously cleaned unetched ITO coated glass substrate by spin-coating at the same rpm and keeping other parameters the same as that of the device. AFM Characterization of the device was performed in non-contact mode with a scan rate of 0.3 nm^2/s to get the best result. Fig. 6.12 shows the non-contact AFM image of the device in a 7.5×7.5 μm^2 area. The average roughness of the device on the whole area is 70 nm, and the red circle and rectangle show the holes in the device. Due to these holes and also the porous nature of the molecular assembly on the surface of the thin film, a high leakage current was there.

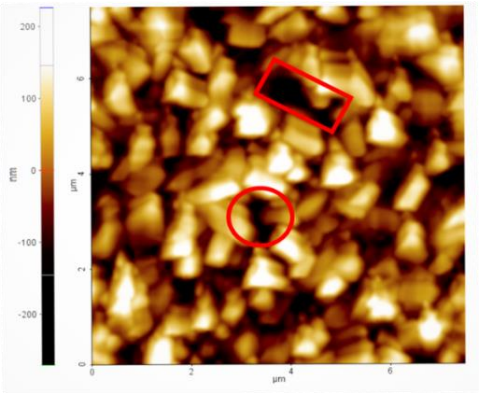

Fig. 6.12 AFM image of the device taken in the non-contacting mode with a scan speed of 0.3 nm^2/Sec. The circle and rectangle show the holes on the surface, which are responsible for leakage current.

The negative differential behavior of the device can be explained by using the model of reduction of the molecule. Azobenzene has the tendency to undergo reduction by accepting an electron [Lee et al., 2014]. When positive voltage was applied to the device, the molecule reduced by accepting electrons on the azo group, which was acting as a quantum well. Due to reduction, the current decreased, so the peak and valley can be seen on the current vs. voltage plot. After a certain high electric field, the electrons can gain enough energy to overcome the quantum well, so the current starts increasing. The current flow was associated with filament formation by making a conducting path. So when a negative voltage is applied, the device makes conducting filaments through the film and reaches the compliance current (10mA).

6.4 Conclusion

In summary, a new dinuclear monoorganostannoxane $[(RSn^{IV})_2(\mu\text{-}OH)(\mu\text{-}OMe)Cl_4]\cdot CH_3OH$ (R = 2-phenylazophenyl) **(4)** has been synthesized using an intramolecular coordination approach and structurally characterized by single-crystal x-ray crystallography. Complex **4** is further characterized by FTIR, UV-Vis, TGA, ^1H, ^{13}C, and ^{119}Sn NMR spectroscopy. Single-crystal X-ray diffraction analysis of **4** reveals a simultaneous bridging coordination mode of µ-hydroxy and µ-methoxy ligands, which is uncommon in monoorganostannoxanes. TD-DFT studies on complex **4** revealed that the transition at 373 nm is a two equal probability π-π^* transitions from HOMO to LUMO+1 and HOMO-1 to LUMO based on 2-phenylazophenyl moiety. The changes in frontier orbitals, torsion in the aromatic rings, and HOMO-LUMO gaps in the singly reduced species of complex **4** are suggested the NDR behavior in this molecule. Further, I-V characteristic studies performed on the device made using **4** were found to exhibit excellent NDR behavior in the region of 1.5V to 2.5V. Observation of NDR behavior is unique so far amongst organostannoxanes and should provide encouragement to explore this area further.

…